

# *Chandra* Confirmation of a Pulsar Wind Nebula in DA 495

Z. Arzoumanian<sup>1,2</sup>

zaven@milkyway.gsfc.nasa.gov

S. Safi-Harb<sup>3</sup>

T. L. Landecker<sup>4</sup>

R. Kothes<sup>4,5</sup>

and

F. Camilo<sup>6</sup>

## ABSTRACT

As part of a multiwavelength study of the unusual radio supernova remnant DA 495, we present observations made with the *Chandra X-ray Observatory*. Imaging and spectroscopic analysis confirms the previously detected X-ray source at the heart of the annular radio nebula, establishing the radiative properties of two key emission components: a soft unresolved source with a blackbody temperature of 1 MK consistent with a neutron star, surrounded by a nonthermal nebula 40'' in diameter exhibiting a power-law spectrum with photon index  $\Gamma = 1.6 \pm 0.3$ , typical of a pulsar wind nebula. The implied spin-down luminosity of the neutron star, assuming a conversion efficiency to nebular flux appropriate to Vela-like pulsars, is  $\sim 10^{35}$  ergs s<sup>-1</sup>, again typical of objects a few tens of kyr old. Morphologically, the nebular flux is slightly enhanced along a direction, in

---

<sup>1</sup>CRESST and X-ray Astrophysics Laboratory, NASA-GSFC, Greenbelt, MD 20771.

<sup>2</sup>Universities Space Research Association, Columbia, MD 21044.

<sup>3</sup>Canada Research Chair. Department of Physics and Astronomy, University of Manitoba, Winnipeg, MB, R3T 2N2, Canada.

<sup>4</sup>National Research Council of Canada, Herzberg Institute of Astrophysics, Dominion Radio Astrophysical Observatory, Penticton, British Columbia, V2A 6J9, Canada.

<sup>5</sup>Department of Physics and Astronomy, University of Calgary, Calgary, AB, Canada.

<sup>6</sup>Columbia Astrophysics Laboratory, Columbia University, New York, NY 10027.

projection on the sky, independently demonstrated to be of significance in radio polarization observations; we argue that this represents the orientation of the pulsar spin axis. At smaller scales, a narrow X-ray feature is seen extending out 5'' from the point source, a distance consistent with the sizes of resolved wind termination shocks around many Vela-like pulsars. Finally, we argue based on synchrotron lifetimes in the estimated nebular magnetic field that DA 495 represents a rare pulsar wind nebula in which electromagnetic flux makes up a significant part, together with particle flux, of the neutron star's wind, and that this high magnetization factor may account for the nebula's low luminosity.

*Subject headings:* ISM: individual (DA 495, G65.7+1.2) — radiation mechanisms: nonthermal — stars: neutron — supernova remnants — X-rays: ISM

## 1. Introduction

With the *Chandra X-ray Observatory's* first glimpse of the Crab pulsar (Weisskopf et al. 2000), a new window was opened onto the interactions of neutron stars with their surroundings. Rotation-powered pulsars drive outflows of particles and electromagnetic energy into the immediate environment; depending primarily on the pulsar's age, this environment might simply be the interstellar medium or, in the case of young, energetic pulsars, the circumstellar debris of the supernova explosion that accompanied the birth of the neutron star. The astrophysical value of these interactions lies in their uniqueness as a probe of the content of pulsar winds, which originate in the incompletely understood magnetospheres of neutron stars, and of the physics of particle acceleration and shock mixing of relativistic and non-relativistic fluids. In contrast to the optical and radio observations that provided early insights into these phenomena, X-ray studies, in particular with *Chandra's* unequalled angular resolution, sample the properties of energetic and short-lived particles nearest the accelerating engines that produce them.

In the class of filled-center supernova remnants (SNRs), the bulk of the radiation from a remnant can be traced back energetically to the rapidly rotating neutron star at its core, with emission from the shocked neutron star wind often defining a pulsar wind nebula (PWN). Shell-type remnants, by contrast, expend the energy of the supernova explosion's blast wave. Evidence for the transfer of a neutron star's rotational kinetic energy to its surroundings is provided by the axisymmetric structures—arcs, rings, tori, and jets—seen in high-resolution X-ray images of the environs of a number of pulsars. Together with amorphous nonthermal emission also found around energetic pulsars, these structures are brought to light through synchrotron radiation by the pulsar's ultrarelativistic particle wind where it is confined and

perturbed by the surrounding medium; see, e.g., Gaensler & Slane (2006) for a review of PWNs. The morphological and spectral properties of PWNs carry valuable information about the physical mechanisms of energy transfer, the local conditions (particle densities, flow velocities, magnetic field strengths, etc.), and the nature of the particle-accelerating central engine.

Although its identification as a pulsar wind nebula is now virtually certain, the DA 495 radio nebula (G65.7+1.2; Landecker & Caswell 1983) is highly unusual: its morphology is distinctly annular, with a radial profile that rises rapidly from a central emission deficit (the “hole”) then falls gradually with increasing distance from the center; see Figure 1 for a contour map, and Kothes et al. (2008) for a detailed discussion of the radio properties. We described in an earlier paper (Arzoumanian et al. 2004; hereafter, ASLK04) X-ray observations of DA 495 that revealed the central engine apparently powering the radio nebula, the *ROSAT* source 1WGA J1952.2+2925, and provided some evidence for extended X-ray emission consistent with a PWN. To confirm the existence of a high-energy nebula, and because lingering doubts remained about a possible “thick shell” thermal origin for the radio annulus (Velusamy et al. 1989), we set out to perform with *Chandra* an X-ray observation sensitive to compact nonthermal structures as a means of strengthening the identification of DA 495 as a PWN, through the detection in particular of jets, toroidal structures, or other markers of large-scale axial symmetry, such as those seen around the Crab, Vela, and similar pulsars.

## 2. Observations

The *Chandra* observation of DA 495 was carried out on 2002 December 9. Anticipating the need for a large field of view—to search for X-ray emission from the entire  $\sim 20'$ -diameter radio nebula—we used the Advanced CCD Imaging Spectrometer (ACIS) instrument with the putative pulsar, 1WGA J1952.2+2925 (see ASLK04), placed at the aimpoint of the I3 CCD. The 4-chip ACIS-I array neatly captured most of the radio extent of DA 495 within its  $16.9'$  square field of view. Two additional CCDs, the front-illuminated chips ACIS-S2 and -S4 were also activated to provide a measure of the X-ray background in fields adjacent to the radio nebula; ultimately, only S2, which lies closer to the telescope’s optical axis, was used.

X-ray photon events were acquired in timed-exposure (TE) readouts of the ACIS CCDs, and telemetered to the ground in Very Faint mode. The starting points for our analyses were event lists, aspect solutions, and other standard data products resulting from the third reprocessing (REPRO-III) of raw data at the *Chandra* X-ray Center. We used the CIAO software package (version 3.3.0.1; Fruscione et al. 2006) and associated calibration database

(CalDB version 3.2.3) for reduction of the ACIS data.

### 3. Results

Following standard data preparation procedures<sup>1</sup> for filtering (e.g., rejection of events due to particle background rather than cosmic X-rays), effective area and energy calibrations, and mapping of detector to sky coordinates, final ACIS photon event lists were used to cumulate images, spectra, and lightcurves for further analysis. For an observation duration of 25,160 s, a total filtered exposure of 24,843 s was acquired. We found that photon events outside the 0.6–7 keV energy band were consistent with background and provided little useful information; unless noted otherwise, all of the following discussion refers to analysis and results in this energy range.

#### 3.1. Image Analysis

The map of X-ray counts on the sky for all CCDs active during the 25 ks *Chandra* observation, binned by a factor of 16, is shown in Figure 1, with radio contours superposed. The basic result of earlier *ROSAT* and *ASCA* observations (ASLK04), that an X-ray source lies near the center of the DA 495 annulus, is readily confirmed (source ‘A’). ASLK04 argued further that the *ASCA* images were consistent with a combination of soft emission from a compact source and harder emission from a nebula barely resolved by the available  $\gtrsim 1'$  angular resolution. The leap to *Chandra*’s arcsecond-level imaging upholds this conclusion as well, demonstrating however (as discussed below) that it was fortuitously reached: the extent of the diffuse X-ray emission is too small to have been resolved by *ASCA*. Instead, a small number of unrelated nearby sources were blended by the *ASCA* point-spread function, giving the appearance of extended nebulosity.

To allow for morphological analysis with the best available angular resolution, we formed ACIS images with pixel randomization (used by default in standard CIAO data reduction to avoid spatial digitization effects) disabled; we also applied the sub-pixel event localization algorithm described by Mori et al. (2001). In practice, we found that these techniques produced no discernible change in the morphology of the diffuse X-ray emission, but yielded a somewhat improved ( $\sim 10\%$ ) concentration of counts onto the point-like source from its

---

<sup>1</sup>Standard procedures are described in CIAO software analysis guides and “threads” available at <http://cxc.harvard.edu/ciao/guides/>.

immediate vicinity. The coordinates of the unresolved source on the sky are (J2000) RA  $19^{\text{h}}52^{\text{m}}17^{\text{s}}.04$ , Dec  $+29^{\circ}25'52''.5$ , good to the nominal *Chandra* astrometric uncertainty of  $0.6''$ .

In the full-resolution ACIS-I image, Figure 2, the X-ray nebulosity is revealed to be  $\sim 40''$  in diameter. The extended emission surrounds the point-like source but is not centered on it. Instead, there is a strong asymmetry, roughly along an east-west line, in both flux and radial extent, with most of the diffuse flux lying to the east of the unresolved source. To quantify this asymmetry, we sum the counts detected within the eastern and western halves of a  $20''$ -radius circle centered on the point source, neglecting the latter's flux by excluding the central  $1''$ -radius circle. Of the 474 counts that define the X-ray nebula and are contained within the larger circle, 314 lie to the east and 160 to the west of the north-south bisector. As shown in Figure 2, we choose an extraction region for spectral analysis that is not centered on the point source, in order to better match the asymmetric shape of the nebula. The background-subtracted countrate within this extraction circle was  $18.4 \pm 1.5$  cts  $\text{ks}^{-1}$ . For the unresolved source, 175 counts were detected in a  $1''$ -radius region centered midway between the two brightest pixels, for a background-subtracted countrate of  $7.0 \pm 1.3$  cts  $\text{ks}^{-1}$ ; the same region was used to accumulate a spectrum. Figure 2 displays the *Chandra* images in two energy bands, with and without smoothing; the softness of the point source relative to the extended emission is evident. Radial surface brightness profiles of the observed emission, in comparison to the *Chandra* point-spread function, are shown in Figure 3.

The low surface brightness of the X-ray nebulosity ( $0.36$  cts  $\text{arcsec}^{-2}$ ) and the brevity of the observation conspire to make difficult the identification of any well-defined structures within the nebula. Smoothing of a raw counts image can increase the significance of faint features if their extents are well-matched to the smoothing scale, but the resulting images can also be misleading if over-interpreted. Nevertheless, we experimented with Gaussian and adaptive smoothing techniques to attempt to discern compact structures such as those exemplified by the Crab nebula. Two candidate features emerge. The first is an apparent arc of emission, resembling an inverted hook, 10 pixels ( $4.92''$ ) in extent and immediately adjacent to the point source: it extends initially to the east and then curves south (Fig. 4). Whether this feature is truly curved is unclear, but it is sufficiently bright in the unsmoothed image (61 counts in a  $15 \times 9$ -pixel elliptical extraction region) relative to the local background (an average of 21 counts in the same elliptical region positioned at four nearby locations) that it is statistically significant at the  $4\sigma$  level. The apparent curvature results from a deficit of counts immediately to the SE of the point source, but statistical fluctuations could account for this deficit.

The second structural detail suggested by the data, near the detection limit for low

surface-brightness features, is slightly enhanced flux along a line (labeled “NE Enhancement” in Fig. 4) extending from the point source to the northeast. In Figure 4, we plot the counts contained within a number of identical rectangular strips, centered on the point source and rotated at  $10^\circ$  intervals. The resulting measurements are found to be roughly consistent with a constant flux, but although the deviations from the mean are not highly significant, the trend is suggestive of an enhancement along the line at  $50^\circ$  north through east. Consistent with the overall east-west asymmetry in the nebular flux, the enhanced emission that may exist to the northeast is clearly nonexistent in the opposite direction, to the southwest of the point source; repeating the counting analysis shown in Figure 4 with a rectangular region that only samples the semicircular region to the east of the point source (out to the same radius) results in a statistically more significant peak at  $50^\circ$ .

While the evidence for this directionally enhanced flux in the *Chandra* data alone is meager, an independent measurement lends support to make it more compelling (cf. Fig. 4). In the work of Kothes et al. (2008; hereafter, KLR+08), a multi-frequency radio polarization study of DA 495 allows for the measurement of its spatially-varying rotation measure. Combined with modeling of the particle densities within the remnant, the orientation of the intrinsic magnetic field can be derived. The result favors a dipolar field oriented at  $50^\circ$ , identically to our NE enhancement, in projection on the sky. Thus, two distinct results point to a preferred direction and the possibility of axisymmetry in the morphology of DA 495.

We note with interest that the two diffuse features, the hook and the NE enhancement, appear to lie in orthogonal directions, suggestive of equatorial and polar structures seen in many PWNs. We discuss this possibility further below.

In our analysis of *ASCA* data (ASLK04) we argued—without prior knowledge of the radio nor *Chandra* results—that a marginally resolved hard source was extended along a NE-SW direction. Figure 4 overlays the innermost *ASCA*-GIS smoothed-intensity contour onto the *Chandra* image. Although the coincidence of the *ASCA* contour with the NE enhancement and radio-derived magnetic axis is striking, *Chandra*’s superior angular resolution reveals a collection of pointlike, hard X-ray sources that collectively account for the elongated *ASCA* feature, which is thus an artifact of the telescope’s optical limitations rather than a true morphological feature.

Aside from the unresolved and diffuse X-ray emission believed to be associated with DA 495, 48 additional sources are seen in the ACIS-I field of view. Two of these lie within the confines of the DA 495 radio nebula but their faintness and spectral properties suggest that they are extragalactic background sources:

CXOU J195217.1+292532 is unresolved, faint (ten counts in a  $3 \times 3$ -pixel area), hard, and

lies  $21''$  south of source A—it is visible in the hard-band images in Figure 2. No counterpart at another wavelength has been cataloged.

CXOU J195217.4+292745 (Source C) consists of nine counts in a  $3 \times 3$ -pixel area, all between 2 and 8 keV, and is coincident with an unresolved feature in radio images. Future high-resolution radio maps will better distinguish between the nebular radio flux of DA 495 and the contribution of source C, a likely background AGN.

A third notable source is the brightest in the field, CXOU J195253.1+292633 (Source B). Astrometric coincidence suggests that it is the X-ray counterpart of the star 2MASS J19525309+2926337.

### 3.2. Spectral Analysis

Spectral analysis was carried out for three source regions: the point source at the heart of DA 495, the surrounding diffuse emission within a  $20''$ -radius circle, and a larger annulus encompassing the brightest parts of the radio nebula to search for thermal X-ray emission associated with a “thick shell” supernova remnant. Suitable background regions, in some cases more than one, were identified for each source region; serendipitous sources were excised and background spectra subtracted from accumulated source spectra prior to fitting with the *Sherpa* software. Results for all spectral fits are summarized in Table 1.

Following the results of KLR+08, we adopt an assumed distance to DA 495 of 1 kpc when estimating luminosities of the various emission components.

#### 3.2.1. Nebula and Point Source

Point-source and nebular spectra were formed using the *psextract* and *specextract* scripts, respectively, with response matrices for the regions of interest generated using the *mkacisrmf* tool. For the point source, a circular extraction region with a radius of 2 pixels ( $\sim 1''$ ), centered midway between the two brightest pixels, was defined to minimize contamination from the nebula, and extracted events were grouped in energy so that a minimum of 15 photons fell into each spectral bin. For the diffuse emission, the extraction circle (Fig. 2) was  $40''$  in diameter and centered  $4''$  to the northeast of the point source; events were grouped to a minimum of 20 counts per energy bin. To allow for consistency checks, two regions were used to estimate the contribution of background emission to the source spectra (see Fig. 1): an annular arc to the north of the nebula with inner and outer radii  $2.1'$  and

2.5' respectively, centered on the point source and extending out to the chip gaps to its east and west; and a circular region (radius 1.2') at the northern corner of the I3 chip, where there is essentially no radio emission from the remnant.

Events contained within the point source region reflect an evidently soft-spectrum origin: just 4 counts were detected in the energy band above 2.5 keV, consistent with the surface brightness of the surrounding diffuse emission, so that the point source is cleanly detected only at low energies (e.g., Fig. 3). A blackbody spectral model adequately describes this emission, with best-fit parameter values that do not depend, to within estimation uncertainties, on which background region is used. In the diffuse emission, there were too few counts to allow for quantitative analysis of any features or sub-regions other than the integrated nebula, which exhibits a hard tail consistent with an absorbed power-law spectral model.

Statistically, the most well-constrained spectral fits were those made for the point-source (blackbody) and diffuse (power-law) emissions simultaneously, with a common interstellar absorption parameter, the neutral hydrogen column density  $N_{\text{H}}$ . We verified that fits to each component separately produced consistent results, finding however that poor statistics prevented measurement of  $N_{\text{H}}$  in either fit alone—even in the simultaneous analysis, the best-fit value  $N_{\text{H}} = (0.23 \pm 0.17) \times 10^{22} \text{ cm}^{-2}$  amounts to an upper limit at the  $2\sigma$  level. Observed and model spectra derived from the simultaneous analysis are shown in Figure 5, together with confidence contours projected onto two-dimensional slices of the full five-dimensional parameter grid. Least squares minimization produced the best fit at a reduced  $\chi^2 \simeq 0.5$  for 27 degrees of freedom.

For the point source, power-law fits were formally acceptable (reduced  $\chi^2 \simeq 0.7$ ), but produced steep spectra (photon indices  $\Gamma \sim 3.5$ ) when  $N_{\text{H}}$  was fixed at the nebular value, and steeper still when  $N_{\text{H}}$  was allowed to vary up to five times the nebular value. We prefer instead thermal models: a blackbody spectrum yields a best-fit temperature of  $0.23_{-0.04}^{+0.06}$  keV (uncertainties are  $1\sigma$  throughout), for a bolometric unabsorbed flux of  $\sim 8 \times 10^{-14} \text{ ergs cm}^{-2} \text{ s}^{-1}$ . The isotropic luminosity of the source is then  $L_{\text{X}} \sim 10^{31} (d/1 \text{ kpc})^2 \text{ ergs s}^{-1}$  for distance  $d$ , implying for a simple blackbody an emitting area with a characteristic radius of  $\sim 0.3 (d/1 \text{ kpc}) \text{ km}$ . This size is consistent with the area of a magnetic polar cap, heated by bombardment of particles accelerated in the magnetosphere, on the surface of a neutron star with a rotation period of several tens of milliseconds (i.e., similar to the Vela pulsar). Propagation effects in stellar atmospheres, however, are believed to significantly distort thermal spectra, making temperature and size estimates unreliable, with pure blackbody fits tending to overestimate temperatures by up to a factor of two depending on the magnetic field strength and composition of the atmosphere.

To investigate the possible impact of an atmosphere, we used the XSPEC NSA model



(Pavlov et al. 1995, Zavlin et al. 1996) to fit the point-source spectrum to presumed emission from the entire stellar surface for nonmagnetic atmospheres as well as  $B = 10^{12}$  and  $10^{13}$  G conditions. For canonical neutron star mass ( $1.4 M_{\odot}$ ) and radius (10 km) assumptions, these fits also provide a distance estimate, as the emitting area seen by a distant observer is fixed. The fits demonstrated that reasonable values of effective surface temperature and distance (shown in Table 1; their implications are discussed in Sec. 4.1) could be inferred from the available data, but we found that the NSA model parameters, effective temperature and overall normalization, were highly covariant with one another in every case, with the  $\chi^2$  surface describing an extended, shallow minimum, precluding a well-bounded measurement of either quantity by itself. The implied luminosity, which depends on both temperature and the normalization, is more reliably constrained. These ill-defined fits are likely the result of poor statistics and the necessarily coarse binning of our observed spectrum; we note, however, that the number of fitting parameters was the same whether we used the NSA models or a simple blackbody, where the latter produced much more robust parameter estimations. Also unlike the blackbody model, the NSA fits all required a hydrogen absorbing column  $N_{\text{H}}$  some three times higher than is supported by our preferred power-law fit to the nebular emission surrounding the point source, as described below. When fit simultaneously,  $N_{\text{H}}$  remains high while the nebular spectrum exhibits unmodeled excess flux at energies  $\lesssim 1$  keV. Attempts to model this excess with additional thermal or nonthermal spectral model components were inconclusive. A deeper observation will be needed to obtain reliable results from neutron star spectral models incorporating atmospheric effects.

For the nebula, the best-fit photon index is  $\Gamma = 1.63 \pm 0.27$ , for 0.5–10 keV and 2–10 keV unabsorbed fluxes of  $2.8 \times 10^{-13}$  and  $1.8 \times 10^{-13}$  ergs  $\text{cm}^{-2}$   $\text{s}^{-1}$ , respectively. The implied 0.5–10 keV isotropic luminosity is  $L_X \simeq 3.3 \times 10^{31} (d/1 \text{ kpc})^2$  ergs  $\text{s}^{-1}$ . These results are largely in line with the *ASCA* measurements reported by ASLK04: the power-law photon index is virtually identical, but the source luminosity derived from *ASCA* data is a factor of 4 higher than the *Chandra* value. This discrepancy is attributable to contamination from the point source and other, unrelated, sources that could not be distinguished from the PWN in the low-angular-resolution *ASCA*-GIS observation. The newly measured  $N_{\text{H}}$  is also consistent with the *ASCA*-derived value; at roughly one-sixth of the full Galactic column density, it supports prior evidence of a small distance to DA 495.

### 3.2.2. Constraints on nebular thermal emission

The only significant diffuse X-ray emission in our *Chandra* image is the nebula that lies within  $\sim 40''$  of the point source, i.e., largely inside the radio “hole.” Fitting this emission to

thermal models yields statistically acceptable results—with, e.g., a bremsstrahlung temperature of 10 keV—but these temperatures are significantly higher than those typically seen in shock-heated supernova remnant interiors ( $\lesssim 3$  keV). A thermal origin of the X-ray nebula is therefore disfavored. More importantly, in a “thick shell” interpretation of the radio emission as being thermal in nature, one would expect significant spatial correspondence between thermal X-ray emission and the bright radio annulus. No X-ray emission in an annular or shell-like structure is seen.

To quantitatively constrain X-ray flux coincident with the radio annulus, we defined an annular region with inner and outer radii of 1.7' and 5.5' respectively, centered on the radio hole, from which to extract source photons. Chip gaps were excluded, and unresolved sources detected by the `vpdetect` tool were removed. To estimate the local background, we defined two regions (as a check on the consistency of the results), one at the northern corner of the I3 chip, and another taking up most of the S2 chip (cf. Fig. 1). The countrates in both of these detector regions were degraded by  $\simeq 15\%$  due to mirror vignetting, resulting in an overestimate of the source flux in a background-subtracted analysis. For the purpose of setting a conservative upper limit on the source flux, however, this is acceptable. We find that the maximum allowable count rate in a diffuse component within the radio-bright annulus is 0.048 cts s<sup>-1</sup> ( $3\sigma$ ) in the 0.5–5 keV band, for a surface brightness  $< 15$  cts arcmin<sup>-2</sup> in 25 ks; corrected for vignetting, the upper limits on photon flux are  $9.5 \times 10^{-5}$  cts cm<sup>-2</sup> s<sup>-1</sup> and  $1.4 \times 10^{-6}$  cts cm<sup>-2</sup> arcmin<sup>-2</sup>.

### 3.3. Timing Analysis

The photon time tagging resolution provided by the *Chandra* CCDs in full imaging mode is 3.2 s, much too poor to allow for a periodicity search for a typical young, rotation-powered pulsar. We did, however, attempt to confirm the putative 10.9 s pulse period we identified, with low statistical significance, in the *ASCA*-GIS data (ASLK04). In Fourier and Bayesian epoch-folding (Gregory & Loredo 1992) analyses, we detected no flux modulations at that, or any other, pulse period  $\gtrsim 10$  s, nor was there any evidence of flaring or other variability in the point source and nebular fluxes.

## 4. Discussion

### 4.1. Thermal properties of the point source and nebula

For the putative pulsar powering the DA 495 nebula, power-law spectral fits are statistically acceptable but yield uncomfortably large photon indices and significantly larger absorption columns than are supported by the spectral fits to the nebula. For nominal fits to the NSA atmosphere models, the bolometric luminosity for an assumed age may be compared with neutron star cooling curves from theory and the blackbody temperatures and luminosities of other pulsars with similar ages (Tsuruta et al. 2002). KLR+08 estimate the age of DA 495 at 20 kyr. For this assumed age, the putative neutron star in DA 495 is underluminous by a factor  $\sim 5$  compared with expectations from standard cooling models,  $L_X \sim 10^{33}$  ergs s $^{-1}$ , assuming the NSA fit results are reliable. The Vela pulsar, among others, is similarly cooler and dimmer than expected (Pavlov et al. 2001). For the blackbody fits, the implied area and temperature are not unreasonable for emission from a heated polar cap, but if the observed flux is dominated by polar caps, any contribution from cooling over the remaining surface would have to be significantly (at least an order of magnitude) less luminous, further exacerbating the discrepancy with cooling theory. It seems reasonable to assume, therefore, that the observed thermal emission is dominated by whole-surface cooling emission and that atmospheric effects are important.

In the context of attempts to describe DA 495 as a “thick shell” SNR (Velusamy et al. 1989), the absence of detectable diffuse thermal emission, either on large scales or as in 3C58 where thermal and nonthermal emission are mixed (Gotthelf et al. 2007), suggests two possibilities. Either no reverse shock has developed, and therefore the PWN is expanding into cool surroundings (presumably ejecta), as in the Crab, or emissions driven by the reverse shock have already dissipated. That a reverse shock, in the former scenario, has not yet produced significant heating of ejecta nor interacted with the PWN in a  $\sim 20$  kyr-old remnant would be somewhat surprising, but the absence of a detectable limb-brightened shell surrounding DA 495 may be significant—the existence of a forward shock is a prerequisite for the formation of a reverse shock. The second case, in which the hot ejecta that signal the passing of a reverse shock have already cooled and dissipated, is difficult to reconcile with a remnant age of just a few tens of kyr. Interaction with a reverse shock would also be expected to significantly compress and distort a PWN (van der Swaluw et al. 2001, Blondin et al. 2001), resulting in asymmetries and, sometimes, spatial offsets between the radio and X-ray emissions such as are found in the Vela and SNR G327.1–1.1 PWNs (Gaensler & Slane 2006). The E-W asymmetry, relative to the central source, in the morphology of the DA 495 X-ray nebula (a hint of which is also evident in the radio morphology) could conceivably be attributed to distortion from passage of a reverse shock, but there is no measurable offset between the

radio and X-ray nebulae, both appearing to be tied to the current pulsar position to within, at worst, the  $\sim 45''$  angular resolution of the available radio images. On balance, it seems unlikely that interaction with a reverse shock has occurred, so that DA 495 is not an evolved SNR. The X-ray results therefore are at odds with a thermal origin for the radio emission; KLR+08 provide further arguments against the thick shell interpretation.

## 4.2. Termination shock

Pulsar wind nebulae are synchrotron structures that depend on the perturbation of free-flowing particles at a standing shock. Of immediate interest in an observed nebula, then, is the possibility of locating this wind-termination shock. Whether the wind is confined by ram pressure induced by the pulsar’s motion or simply ambient pressure in a medium, the shock is associated with a transition from an underluminous (free-flowing) zone to a brighter region. The only feature in our *Chandra* image of DA 495 that approximately matches this description is the “hook” near the central point source: there is a hint of a deficit of X-ray flux where the hook curves southward. If the deficit is significant, the hook may plausibly be associated with the standing shock where the pulsar wind is equatorially confined. The extent of the hook,  $\sim 4''$ , corresponds to a physical size of  $r_{\text{hook}} \sim 0.02 d_1$  pc, where  $d_1 \equiv d/(1 \text{ kpc})$  for distance  $d$ .

An alternative explanation for the hook is that it represents post-shock emission from an equatorial outflow similar to the torus around the Crab pulsar—for which the wind termination shock is more reliably identified with an inner ring of emission—or an associated wisp, as suggested for PSR B1509–58 by Gaensler et al. (2002)<sup>2</sup>. Indeed, the equatorial features seen in most X-ray PWNe are thought to be extended toroidal structures a short distance downstream of the termination shock, rather than “inner ring” markers of the shocks themselves. In these cases, one-half of the observed radius serves as a reasonable estimate of the true wind termination shock radius  $r_s$  (e.g., Kargaltsev et al. 2007). We adopt this interpretation for the DA 495 hook as well, so that  $r_s = r_{\text{hook}}/2 \sim 0.01 d_1$  pc, which is consistent with (the low end of) the equatorial termination shock radii around several Vela-like pulsars (see, e.g., Table 2 of Kargaltsev et al. 2007). The combination of a  $4''$ -radius torus surrounding a  $2''$ -radius ring around an unresolved source would be difficult to disentangle even with *Chandra*. We cannot rule out the possibility that the termination shock is smaller still than we have assumed, that it is unresolved and cannot be distinguished

---

<sup>2</sup>Such wisps may arise from thermal instabilities due to synchrotron cooling (Hester 1998) or compression of particle pairs by magnetic reflections of heavy ions (Gallant & Arons 1994).

from the point source. The Crab’s inner ring is detected with surface brightness at least as high as the downstream torus—in our dataset, the 4 counts above 2.5 keV within the point-source region represent a surface brightness 50% higher than that in the hook for the same energy band, and Poisson fluctuations could allow an even higher unresolved nonthermal flux. Nevertheless, our estimate of  $r_s$  is at worst a useful upper limit: no known PWNs have estimated termination-shock radii smaller than 0.01 pc, and arguments derived below from  $r_s$  estimates generally require an upper limit in any case.

Given, then, the tentatively identified shock radius, a constraint on the spin-down luminosity of the pulsar is available through pressure-balance,

$$\dot{E} = 4\pi cr_s^2 P_{\text{PWN}}/f_\Omega, \quad (1)$$

where  $P_{\text{PWN}}$  is the nebular pressure, and the factor  $f_\Omega$  accounts for a non-isotropic wind; a value  $f_\Omega \simeq 3/2$  corresponding to an equatorially-dominant wind is typically assumed (see, e.g., Bogovalov & Khangoulyan 2002). Assuming equipartition between magnetic and particle pressures,  $P_{\text{PWN}}$  may be estimated from the radio-derived average magnetic field,  $B_{\text{neb}} \simeq 1B_1$  mG (KLR+08, and see Sec. 4.4), where  $B_1 \equiv B/(1 \text{ mG})$ , such that  $P_{\text{PWN}} \simeq 8 B_1^2 \times 10^{-8} \text{ erg cm}^{-3}$ . The resulting  $\dot{E}$  is  $2 d_1^2 B_1^2 \times 10^{37} \text{ ergs s}^{-1}$ . An independent estimate of  $\dot{E}$  is available, in principle, by assuming an efficiency of conversion from spin-down to nebular luminosity,  $\eta \equiv L_X/\dot{E}$ , between  $10^{-5}$  and  $10^{-3}$ , consistent with the PWNs seen around Vela-like pulsars (i.e., those with characteristic ages of 10–30 kyr; Kargaltsev et al. 2007). For our measured 0.5–8 keV nebular luminosity,  $L_X = 2.9 \times 10^{31} \text{ ergs s}^{-1}$ , the implied  $\dot{E}$  lies between  $3 \times 10^{34}$  and  $3 \times 10^{36} \text{ ergs s}^{-1}$ , well within the range of known Vela-like pulsars, but a factor of 10–1000 below the value implied by the putative termination shock radius, which is also consistent with the same set of pulsars. Reconciliation of these  $\dot{E}$  estimates would require one of the following to hold true: (1) the termination shock is actually unresolvable ( $\lesssim 1''$ ) and  $\log \dot{E} \lesssim 36$ ; (2)  $\dot{E}$  is indeed high ( $\log \dot{E} \sim 37$ ) as required by the hook, but the conversion efficiency  $\eta$  to nebular flux is only a few times  $10^{-6}$ ; (3) the pulsar wind flows predominantly into a solid angle much less than assumed by the factor  $f_\Omega$ , reducing the pressure-derived  $\dot{E}$  estimate by an order of magnitude or more; (4) the nebular pressure estimate, which is based on radio-wavelength measurements made at radii beyond the extent of the observed X-ray nebula, is too high by an order of magnitude or more, and  $\log \dot{E} \sim 35$ . Option (1) is possible, as argued above, but would place DA 495 outside the company of Vela-like PWNs in its termination shock radius, while option (2) is difficult to entertain because a  $10^{37} \text{ ergs s}^{-1}$  pulsar would seem likely to be detectable as a radio or gamma-ray pulsar, or both, and would be significantly younger than the estimated 20 kyr age of DA 495. Options (3) and (4), or a combination of them, therefore appear most reasonable. The assumption of equipartition in deriving  $P_{\text{PWN}}$ , in particular, may be suspect: in the PWN model of Kennel & Coroniti (1984), equipartition holds only at a single post-shock distance that depends on the ratio

of electromagnetic to particle flux in the wind, with particle pressure dominating closer in and magnetic pressure further out. Typical equipartition radii are  $5\text{--}20r_s$ . Because the radio nebula is brightest at  $\gtrsim 30r_s$ , the pressure inferred from the radio-derived magnetic field may significantly overestimate the confining pressure at the wind termination shock. For pressures that correspond to equipartition field strengths comparable to those of PWNs around other Vela-like pulsars,  $B_1 \simeq 0.1$ , the two methods of estimating  $\dot{E}$  are brought in line.

### 4.3. Morphology and connection to radio properties

Lending further credence to the identification of DA 495 as a PWN is the fact that the combination of a soft point source surrounded by a hard nebula is not uncommon among pulsars that are tens of kyr old. In particular, the Vela pulsar, PSR B1706–44, and G189.22+2.90 (IC443) all share this property (Pavlov et al. 2001, Gotthelf et al. 2002, and Gaensler et al. 2006, respectively), where Vela and B1706–44 inflate wind nebulae confined by the ambient medium while IC443’s supersonic motion produces a ram-pressure confined nebula. Intriguingly, sensitive radio imaging and polarimetry of the Vela supernova remnant has shown (Dodson et al. 2003) that the pulsar and PWN lie within a radio emission depression straddled by a pair of symmetric polarized lobes, both of which are also features of DA 495.

That the pulsar wind in DA 495 is confined by ambient rather than ram pressure is supported by two observations: (1) the X-ray PWN morphology does not resemble a bow shock or narrow “trail” of emission (cf. PSR B1957+20; Stappers et al. 2003), and (2) despite the spatial offset of the point source from the center of the radio annulus, a low velocity—at most a few tens of  $\text{km s}^{-1}$ —is suggested by the anchoring of the polarized radio emission (which is due to long-lived particles injected soon after the pulsar was born) at the current position of the pulsar (KLR+08). The radio hole, then, may plausibly be attributed to an absence of synchrotron-emitting particles in a region similar to the so-called optical “bays” seen in the Crab nebula (Fesen et al. 1992). Regrettably, the spacecraft roll angle during the observation was such that the coordinates of the radio hole largely fell upon one of the chip gaps in the ACIS-I array (Fig. 1), resulting in poor sensitivity to any X-rays from the hole region.

Virtually all known PWNs are axisymmetric in their morphologies, and many—e.g., 3C58 (Slane et al. 2004) and the PWN in the G54.1+0.3 SNR (Lu et al. 2002)—are notably elongated in X-rays along their apparent pulsar spin axis directions. The only feature in the DA 495 X-ray PWN that hints at axisymmetry is the putative NE enhancement; its existence

depends on just a dozen or so detected photons in our *Chandra* image, but the symmetry axis that it suggests is supported by an independent radio measurement. Whether the NE enhancement in DA 495 represents an elongation of the PWN’s faint outer reaches or is simply a brightened region is difficult to establish conclusively from the available data. If its orientation does correspond to the spin axis of the neutron star, the feature may plausibly be explained by increased synchrotron lifetimes in a weak axial field relative to the equatorial direction, or perhaps a variation on the proposed process (Lyubarsky 2002, Del Zanna et al. 2004) that collimates axial outflows into the narrow relativistic jets that appear to emanate from the rotational poles of the Vela pulsar, B1706–44, and many others.

Aside from orientation, the radio model of KLR+08 provides further evidence in support of the NE enhancement in DA 495: the radio polarization-derived inclination of the magnetic field vector to the line of sight,  $\sim 55^\circ$ , shows the field pointing away from us to the SW, so that the *Chandra* brightening to the NE (and perhaps much of the overall E-W asymmetry in X-ray flux) is consistent with Doppler boosting, especially given the relativistic flow speeds implied by the synchrotron cooling time (see below). If the “hook” to the east and south represents a portion of the wind termination shock or an equatorial torus, then the DA 495 X-ray structure would be reminiscent of the PWN in G54.1+0.3 and other objects (e.g., Ng & Romani 2004) in that both the equatorial and polar (jets, in most cases) structures, ostensibly orthogonal to one another, are brightened on the same side of the pulsar, a situation difficult to reconcile entirely with Doppler boosting.

Comparison of the radio and X-ray spectra is also instructive. KLR+08 find that the broadband radio spectrum of DA 495 shows a break near 1.3 GHz; the measured spectral slopes below and above the break are  $\alpha_{\text{Rlo}} = -0.45 \pm 0.2$  and  $\alpha_{\text{Rhi}} = -0.87 \pm 0.1$  respectively (defined such that flux  $S$  at frequency  $\nu$  is expressed as  $S \propto \nu^\alpha$ ). KLR+08 weigh the available evidence bearing on the origin of the break, whether it is due to synchrotron cooling or is intrinsic to the spectrum of radiating particles injected by the pulsar. A key discriminant is the spectrum of the X-ray PWN, which suggests through the following reasoning that the break is in fact due to cooling and not a consequence of the injected spectrum (see KLR+08 for additional arguments). The radiative lifetimes of synchrotron-emitting particles are such that the bulk of the observed radio emission must arise from particles that were injected into the nebula soon after the pulsar was born, when spin-down luminosity was at its peak. In contrast, the X-ray emission is dominated by particles that have only recently been injected (see below). Thus, if the origin of the break lies in synchrotron cooling, if the injected particle spectrum is unbroken between the radio and X-ray bands, and finally if the injected spectrum has not changed substantially since the pulsar was born (despite declining in particle luminosity) then one expects that the X-ray spectral slope  $\alpha_X \equiv 1 - \Gamma = -0.63 \pm 0.27$  should lie somewhere between the two radio spectral slopes, and perhaps closer to  $\alpha_{\text{Rlo}}$ .

This is indeed observed, albeit with large combined uncertainties. The general agreement in spectral slopes suggests that the conditions above are not violated. For example, the existence of an injected break at an intermediate frequency between radio and X-ray can be discounted at the  $2\sigma$  level if it is to resemble those with spectral slope differences  $\Delta\alpha > 0.5$  seen at tens of GHz in three filled-center SNRs (G29.7–0.3, 3C58, and G16.7+0.1; see KLR+08). Similarly, attribution of the observed break at 1.3 GHz to the injected spectrum is formally allowed but somewhat contrived: it would require that  $\alpha_X$ ,  $\alpha_{\text{Rhi}}$ , and  $|\alpha_{\text{Rhi}} - \alpha_{\text{Rlo}}|$  *all* take on values at or beyond their  $1\sigma$  uncertainties so that the X-ray slope is at least as steep as the high-frequency radio slope, and that the magnitude of the 1.3 GHz break is greater than 0.5, for consistency with other injected breaks in the radio band.

#### 4.4. Wind magnetization

Based on the conclusion that the 1.3 GHz spectral break is due to radiation losses, KLR+08 compare the energetics of DA 495 with those of other PWNs and infer a nebular field strength of  $B_{\text{neb}} \sim 1.3$  mG, a value that exceeds the Crab Nebula’s magnetic field by a factor of four. In addition to the radio probes, such as rotation measure, of  $B_{\text{neb}}$ , an independent determination is possible in principle through steepening of the X-ray emission spectrum with increasing radial distance from the pulsar, but because of the short *Chandra* exposure and low surface brightness of DA 495 in X-rays, a significant measurement was not possible. The vastly different sizes of the X-ray and radio nebulae suggest, however, that synchrotron cooling is very efficient, consistent with the high field derived by KLR+08—the Crab Nebula, for instance, has a radio-to-X-ray size ratio of roughly 3.3, whereas for DA 495 the ratio is  $> 25$ . Because there is substantial uncertainty in the value of  $B_{\text{neb}}$ , however, we assume a value of 1 mG and carry through scalings with  $B_1 \equiv B/(1 \text{ mG})$  when estimating derived quantities.

The synchrotron lifetime of particles emitting at energy  $\epsilon$  keV in a magnetic field  $B$   $\mu\text{G}$  is  $\tau_{\text{synch}} = 39B^{-3/2}\epsilon^{-1/2}$  kyr. For a 1 mG field and emission at  $\epsilon = 1.5$  keV, the radiating lifetime is  $\tau_{\text{synch}} = 1 B_1^{-3/2}$  yr. Thus, the DA 495 PWN imaged with *Chandra* is dominated by particles roughly one year old. The velocity necessary to traverse the  $\gtrsim 20''$ , or  $0.1 d_1$  pc, radius of the nebula within the radiating lifetime is  $0.33 B_1^{3/2} c$ . Lu et al. (2002) find a velocity a substantial fraction of  $c$  for the G54.1+0.3 PWN in the flow immediately downstream of the termination shock; at larger post-shock distances, a velocity of  $\sim 0.01c$  has been estimated for PSR B1046–58 (Gonzalez et al. 2006). In the case of DA 495, the relativistic flow must extend to a great distance post-shock, given that the hook feature provides a reliable upper bound on the termination shock radius  $r_s$  at roughly one-tenth the PWN radius.



Relativistic bulk velocity at a large downstream distance has been inferred for a linear feature in the N157B PWN (Chen et al. 2006), but is thought to arise for that object from strong pressure confinement due to a nearby dense cloud. In the absence of such external influence, the work of Kennel & Coroniti (1984) suggests that relativistic bulk motion at large radii is only possible for values of the “magnetization parameter,” the ratio of electromagnetic to particle energy flux in the pulsar wind, of  $\sigma \simeq 0.3$  which, we argue, applies to DA 495. By contrast, for G54.1+0.3,  $\sigma = 0.06$ , while for the Crab it is smaller still,  $\sigma = 0.003$ . In fact, most estimates of  $\sigma$  to date have found that the observed PWNs are driven by strongly particle-dominated winds (e.g., Petre et al. 2007). A notable exception is the Vela X-ray PWN, for which Helfand et al. (2001) argue that  $\sigma$  is nearly unity, based on the *Chandra*-resolved termination shock and an earlier estimate of the nebular magnetic field. Sefako & de Jager (2003) reach a similar conclusion from modeling of the broadband spectrum. Thus, DA 495 provides, potentially, a second example of a pulsar wind in which Poynting and particle flux appear to be comparable. This conclusion is based on an inferred nebular magnetic field and the observed size of the X-ray PWN; it is worth keeping in mind that spin-down luminosity considerations suggest that the nebular pressure, and thus magnetic field strength, in the X-ray nebula may be smaller than implied by the radio  $B$ -field measurement made at larger distances from the neutron star, underscoring the need for a direct measurement of synchrotron lifetimes through future, high-sensitivity spectroscopy of the X-ray nebula to constrain the burn-off rate via radial steepening of the spectrum.

Importantly, Kennel & Coroniti (1984) show that, naturally, particle dominated winds are necessary for efficient conversion of wind luminosity to synchrotron luminosity. Gotthelf (2004) has pointed out that pulsars with spin-down luminosity less than  $\simeq 4 \times 10^{36}$  ergs s<sup>-1</sup> host substantially dimmer PWNs than their more luminous counterparts. It is tempting to speculate that the magnetization fraction  $\sigma$  varies either with spin-down luminosity or with time such that older, less luminous pulsars produce dim nebulae because Poynting flux contributes substantially to their winds. Current understanding of magnetospheric physics for rotation-powered pulsars argues for a strongly field-dominated wind at the light-cylinder,  $\sigma_{\text{LC}} \sim 10^4$ . The much smaller measured values  $\sigma \lesssim 0.01$  in PWNs imply conversion to a strongly particle-dominated wind by the time the flow reaches the termination shock, at least for the youngest and most energetic pulsars. Candidate mechanisms for effecting this conversion have been proposed (Contopoulos & Kazanas 2002, Contopoulos 2007), but confrontations with observation have not yet been possible. If future PWN studies confirm present suggestions that the winds of Vela-like pulsars emerge from confinement with  $\sigma$  of order unity, the implied reduction in the efficacy of the conversion mechanism for older, less luminous pulsars will be an important test of these models.

## 5. Conclusions

The soft spectrum of the unresolved source near the center of the DA 495 radio nebula, its implied blackbody temperature and luminosity, and its lack of variability on timescales of a few seconds through the 25 ks duration of the observation are highly suggestive of emission from the surface of an isolated neutron star. Taken together with the properties of the surrounding extended, nonthermal emission, no doubt remains that DA 495 is a pulsar wind nebula, driven by the rotation-powered magnetosphere of a neutron star. Its unusual radio characteristics can be explained as the result of aging in the absence of any evident interaction with the supernova explosion's reverse shock, such that DA 495 presents a valuable example of a pristine PWN at an advanced age.

We thank the anonymous referee for a rigorous review that resulted in a much-improved manuscript. Support for this work was provided by the National Aeronautics and Space Administration through *Chandra* Award Number GO3-4092A issued by the *Chandra* X-ray Observatory Center, which is operated by the Smithsonian Astrophysical Observatory for and on behalf of the National Aeronautics and Space Administration under contract NAS8-03060. SSH is supported by the Natural Sciences and Engineering Research Council (NSERC) of Canada and the Canada Research Chair program. The CGPS is a Canadian project with international partners and is supported by the Natural Sciences and Engineering Research Council (NSERC).

## REFERENCES

- Arzoumanian, Z., Safi-Harb, S., Landecker, T. L., & Kothes, R. 2004, *ApJ*, 610, L101 (ASLK04)
- Blondin, J. M., Chevalier, R. A., & Frierson, D. M. 2001, *ApJ*, 563, 806
- Bogovalov, S. V. & Khangoulyan, D. V. 2002, *Astronomy Letters*, 28, 373
- Chen, Y., Wang, Q. D., Gotthelf, E. V., Jiang, B., Chu, Y.-H., & Gruendl, R. 2006, *ApJ*, 651, 237
- Contopoulos, I. 2007, *A&A*, 466, 301
- Contopoulos, I. & Kazanas, D. 2002, *ApJ*, 566, 336
- Del Zanna, L., Amato, E., & Bucciantini, N. 2004, *A&A*, 421, 1063

- Dodson, R., Lewis, D., McConnell, D., & Deshpande, A. A. 2003, MNRAS, 343, 116
- Fesen, R. A., Martin, C. L., & Shull, J. M. 1992, ApJ, 399, 599
- Fruscione, A., et al. 2006, in Proc. of the SPIE 6270, Observatory Operations: Strategies, Processes, and Systems, ed. D. R. Silva, R. E. Doxsey (Bellingham: SPIE), 62701V
- Gaensler, B. M., Arons, J., Kaspi, V. M., Pivovarov, M. J., Kawai, N., & Tamura, K. 2002, ApJ, 569, 878
- Gaensler, B. M., Chatterjee, S., Slane, P. O., van der Swaluw, E., Camilo, F., & Hughes, J. P. 2006, ApJ, 648, 1037
- Gaensler, B. M. & Slane, P. O. 2006, ARA&A, 44, 17
- Gallant, Y. A. & Arons, J. 1994, ApJ, 435, 230
- Gonzalez, M. E., Kaspi, V. M., Pivovarov, M. J., & Gaensler, B. M. 2006, ApJ, 652, 569
- Gotthelf, E. V. 2004, in Bull. of the AAS 36, 917
- Gotthelf, E. V., Halpern, J. P., & Dodson, R. 2002, ApJ, 567, L125
- Gotthelf, E. V., Helfand, D. J., & Newburgh, L. 2007, ApJ, 654, 267
- Gregory, P. C. & Loredano, T. J. 1992, ApJ, 398, 146
- Helfand, D. J., Gotthelf, E. V., & Halpern, J. P. 2001, ApJ, 556, 380
- Hester, J. J. 1998, Memorie della Societa Astronomica Italiana, 69, 883
- Kargaltsev, O., Pavlov, G. G., & Garmire, G. P. 2007, ApJ, 660, 1413
- Kennel, C. F. & Coroniti, F. V. 1984, ApJ, 283, 694
- Kothes, R., Landecker, T. L., Reich, W., Safi-Harb, S., & Arzoumanian, Z. 2008, ApJ, submitted (KLR+08)
- Landecker, T. L. & Caswell, J. L. 1983, AJ, 88, 1810
- Lu, F. J., Wang, Q. D., Aschenbach, B., Durouchoux, P., & Song, L. M. 2002, ApJ, 568, L49
- Lyubarsky, Y. E. 2002, MNRAS, 329, L34

- Mori, K., Tsunemi, H., Miyata, E., Baluta, C. J., Burrows, D. N., Garmire, G. P., & Chartas, G. 2001, in ASP Conf. Ser. 251: New Century of X-ray Astronomy, ed. H. Inoue & H. Kunieda, 576
- Ng, C.-Y. & Romani, R. W. 2004, ApJ, 601, 479
- Pavlov, G. G., Kargaltsev, O. Y., Sanwal, D., & Garmire, G. P. 2001, ApJ, 554, L189
- Pavlov, G. G., Shibano, Y. A., Zavlin, V. E., & Meyer, R. D. 1995, in Proc. of the NATO Adv. Study Inst. on the Lives of the Neutron Stars 3, ed. M. A. Alpar, U. Kiziloglu, J. van Paradijs (Dordrecht: Kluwer), 71
- Petre, R., Hwang, U., Holt, S. S., Safi-Harb, S., & Williams, R. M. 2007, ApJ, 662, 988
- Sefako, R. R. & de Jager, O. C. 2003, ApJ, 593, 1013
- Slane, P., Helfand, D. J., van der Swaluw, E., & Murray, S. S. 2004, ApJ, 616, 403
- Stappers, B. W., Gaensler, B. M., Kaspi, V. M., van der Klis, M., & Lewin, W. H. G. 2003, Science, 299, 1372
- Tsuruta, S., Teter, M. A., Takatsuka, T., Tatsumi, T., & Tamagaki, R. 2002, ApJ, 571, L143
- van der Swaluw, E., Achterberg, A., Gallant, Y. A., & Tóth, G. 2001, A&A, 380, 309
- Velusamy, T., Becker, R. H., Goss, W. M., & Helfand, D. J. 1989, Journal of Astrophysics and Astronomy, 10, 161
- Weisskopf, M. C., et al. 2000, ApJ, 536, L81
- Zavlin, V. E., Pavlov, G. G., & Shibano, Y. A. 1996, A&A, 315, 141

Table 1. Spectral fitting results for X-ray features in DA 495

Emission feature	Model	$N_{\text{H}}$ ( $10^{21} \text{ cm}^{-2}$ )	$\log(T_{\text{eff}})$ (K)	$\Gamma$	$\chi^2/\nu$	Dist. (kpc)	$\log(L_X)$ ( $\text{ergs s}^{-1}$ )
Pt. source	BB	$2.7 \pm 2.0$	$6.40 \pm 0.10$	...	4.4/7	...	31.0
	H (0 G)	$6.4 \pm 0.7$	$\sim 5.8$	...	5.2/7	0.8	31.7
	H ( $10^{12}$ G)	$6.9 \pm 0.9$	$\sim 6.0$	...	5.9/7	1.5	32.3
	H ( $10^{13}$ G)	$6.8 \pm 0.9$	$\sim 6.0$	...	5.1/7	1.4	32.3
Nebula	PL	$1.9 \pm 1.7$	...	$1.58 \pm 0.32$	8.4/19	...	31.4
Pt. source + nebula	BB	$2.3 \pm 1.7$	$6.42 \pm 0.08$	...	12.9/27	...	31.0
	+ PL		...	$1.63 \pm 0.27$		...	31.3
Pt. source + nebula	H ( $10^{13}$ G)	$6.0 \pm 0.7$	$\sim 6.0$	...	18.7/27	1.8	32.4
	+ PL		...	$2.10 \pm 0.24$		...	31.8

Note. — Models BB and PL refer to blackbody and power-law spectra, respectively. H refers to the hydrogen-atmosphere NSA models with magnetic field strengths  $B$  given in parentheses. Luminosities, which for thermal and nonthermal models are bolometric and in the 2–10 keV band, respectively, assume a distance of 1 kpc if the spectral model does not provide an independent estimate.

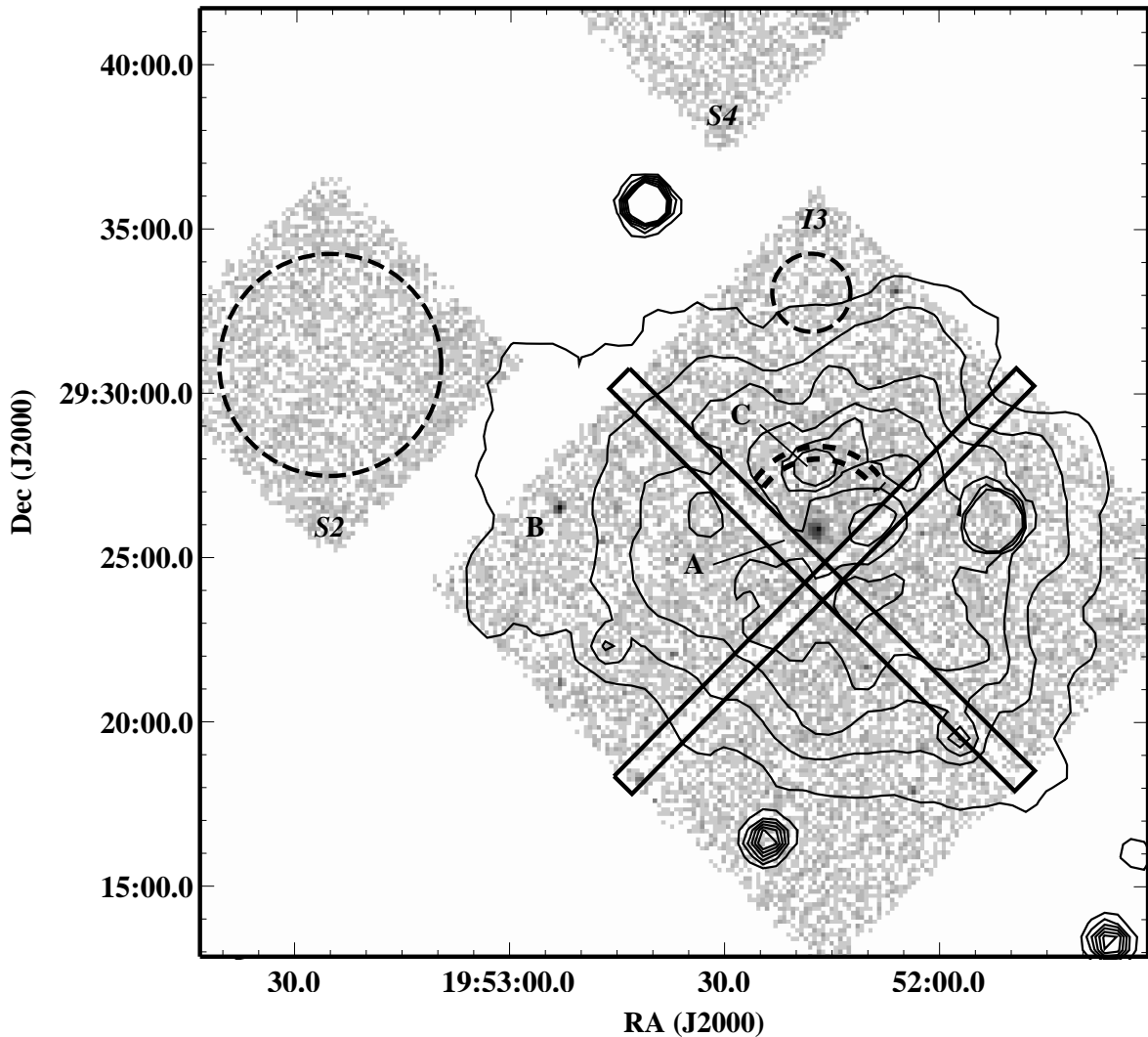


Fig. 1.— *Chandra*-ACIS image of the DA 495 field in a 25 ks exposure: X-ray counts in the 0.6–7 keV band, binned into 8''-pixels, are mapped on a logarithmic grayscale with a maximum of 218 counts. Superposed contours show radio (1.4 GHz Canadian Galactic Plane Survey [CGPS]; see ASLK04) brightness temperatures between 1 and 6 K in 1 K steps. Three X-ray sources are labeled. Source A is the proposed neutron star and wind nebula near the center of DA 495. Source B is a Guide Star Catalog star previously detected by *ROSAT* (1WGA J1952.8+2926). Source C, newly designated CXOU J195217.3+292744, is apparently associated with an unresolved radio enhancement to the north of source A. Event extraction regions used for spectral background estimates are depicted by dashed circles and arcs, while the solid rectangles show regions, affected by gaps between ACIS-I chips, that were excluded from further analysis.

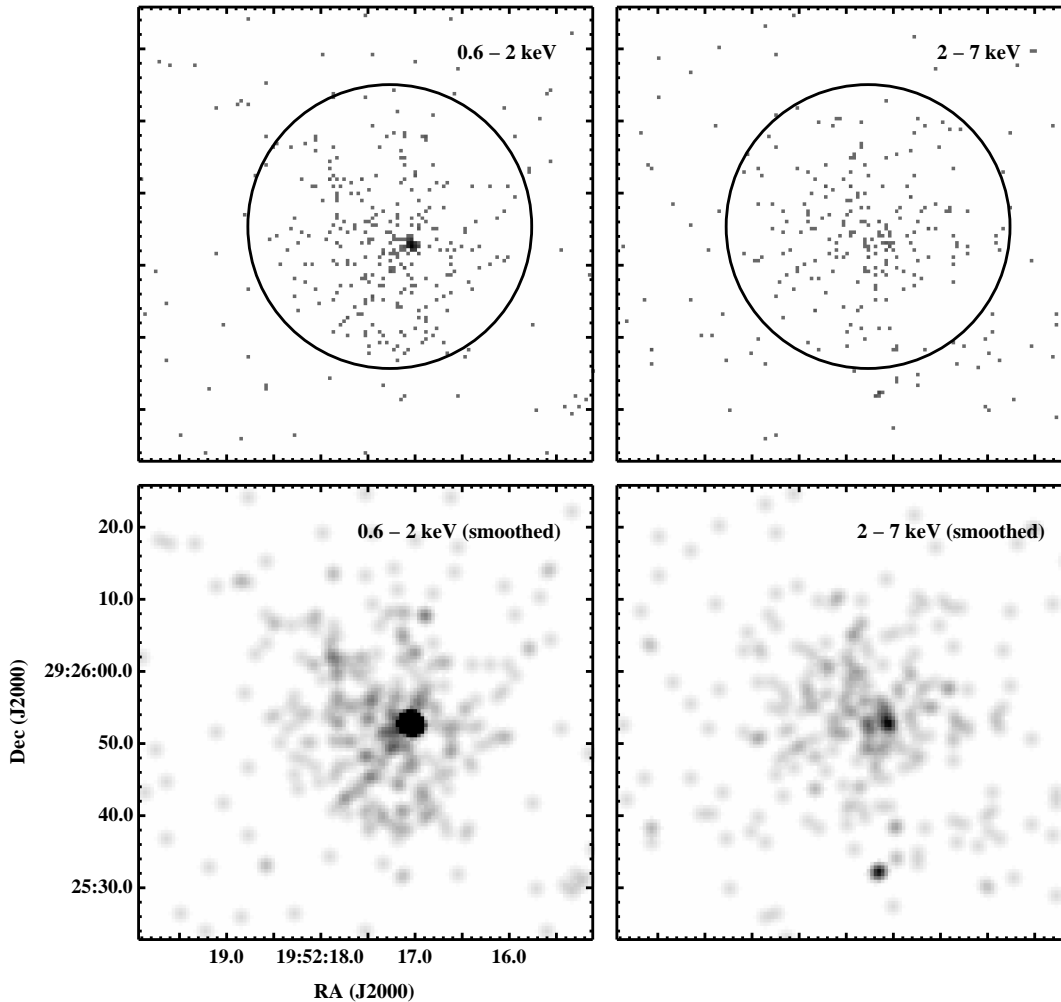


Fig. 2.— *Chandra* images of the central X-ray source in DA 495. *Upper panels:* Raw counts in two energy bands. The grayscale is logarithmic, with a maximum of 50 counts for the central pixel of the unresolved source in the 0.6–2 keV image. Solid circles depict the extraction region for spectral analysis of the nebula; for clarity, the 1''-radius extraction region centered on the point source is not shown. *Lower panels:* The same images smoothed by convolving with a Gaussian of width  $\sigma = 3$  pixels (1.5''). The grayscale is linear, truncated at 0.6 counts pixel<sup>-2</sup>.

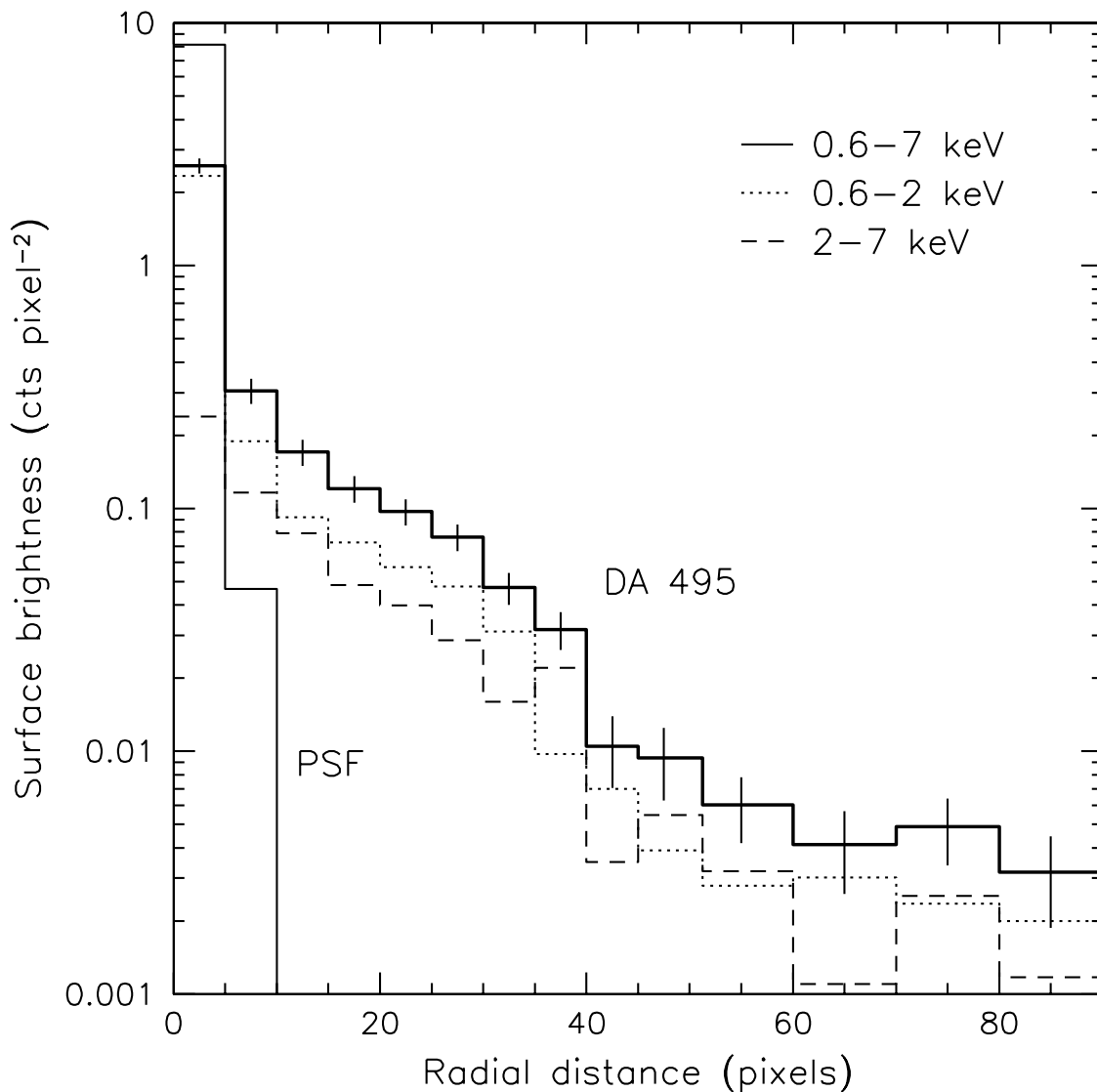


Fig. 3.— Radial surface brightness profiles of the background-subtracted X-ray emission from DA 495 in a series of annuli centered on the unresolved source; the annuli have widths in radius of  $2.5''$  within  $25''$  (50 pixels) of the center, and  $5''$  beyond. Photon energy bands for the dotted, dashed, and solid lines are shown in the legend. The thin solid line corresponds to the radial profile of the *Chandra* point-spread function simulated for a source at the same position as DA 495 on the ACIS-I detector and with the same spectrum. By construction, the integrated area under the two solid curves is the same.



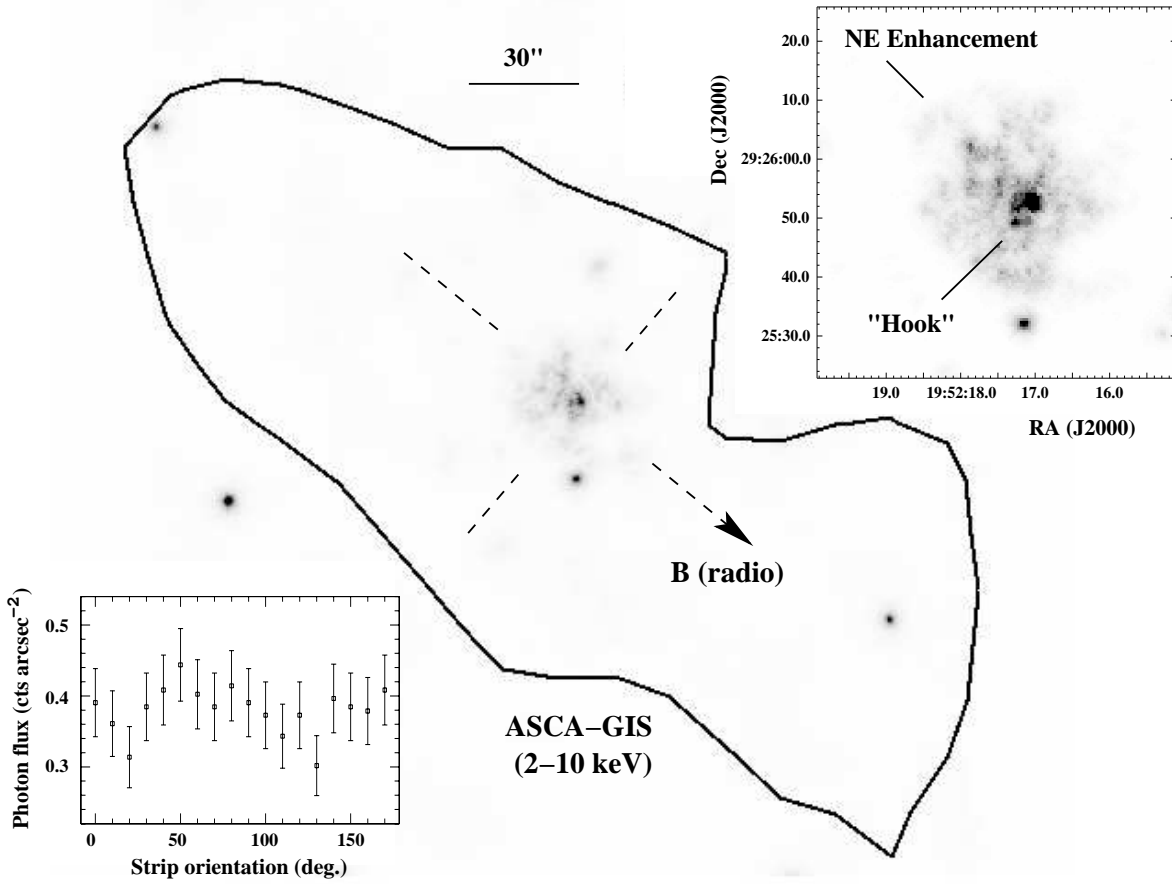


Fig. 4.— Adaptively smoothed 2–8 keV *Chandra* image in the context of an earlier *ASCA* observation and the magnetic field orientation derived from radio polarization measurements. For smoothing, a circular convolution kernel of varying size, requiring a minimum of 5 counts within the kernel diameter, was applied. The single heavy contour depicts the 0.73 counts pixel<sup>-2</sup> level in the smoothed *ASCA*-GIS image (Seq. 57054000, 45” Gaussian smoothing; see ASLK04). *Chandra* resolves a handful of hard X-ray sources that are responsible for the apparent extent of the low-resolution *ASCA* morphology. The dashed lines show the polar (*arrow*) and equatorial directions of the dipole field, on the plane of the sky, inferred from the radio rotation measure (KLR+08), consistent with the “NE Enhancement” in the X-ray PWN and coincidentally in line with the *ASCA* contour. *Inset, upper right*: Close-up of the DA 495 PWN in the 0.6–7 keV band, with adaptive smoothing as above. The greyscale is linear, truncated at 1 count pixel<sup>-2</sup>. *Inset, lower left*: Summed counts within a rectangular extraction region 5 pixels wide and 150 pixels long, centered on the point source but excluding it, as a function of its orientation angle north through east.

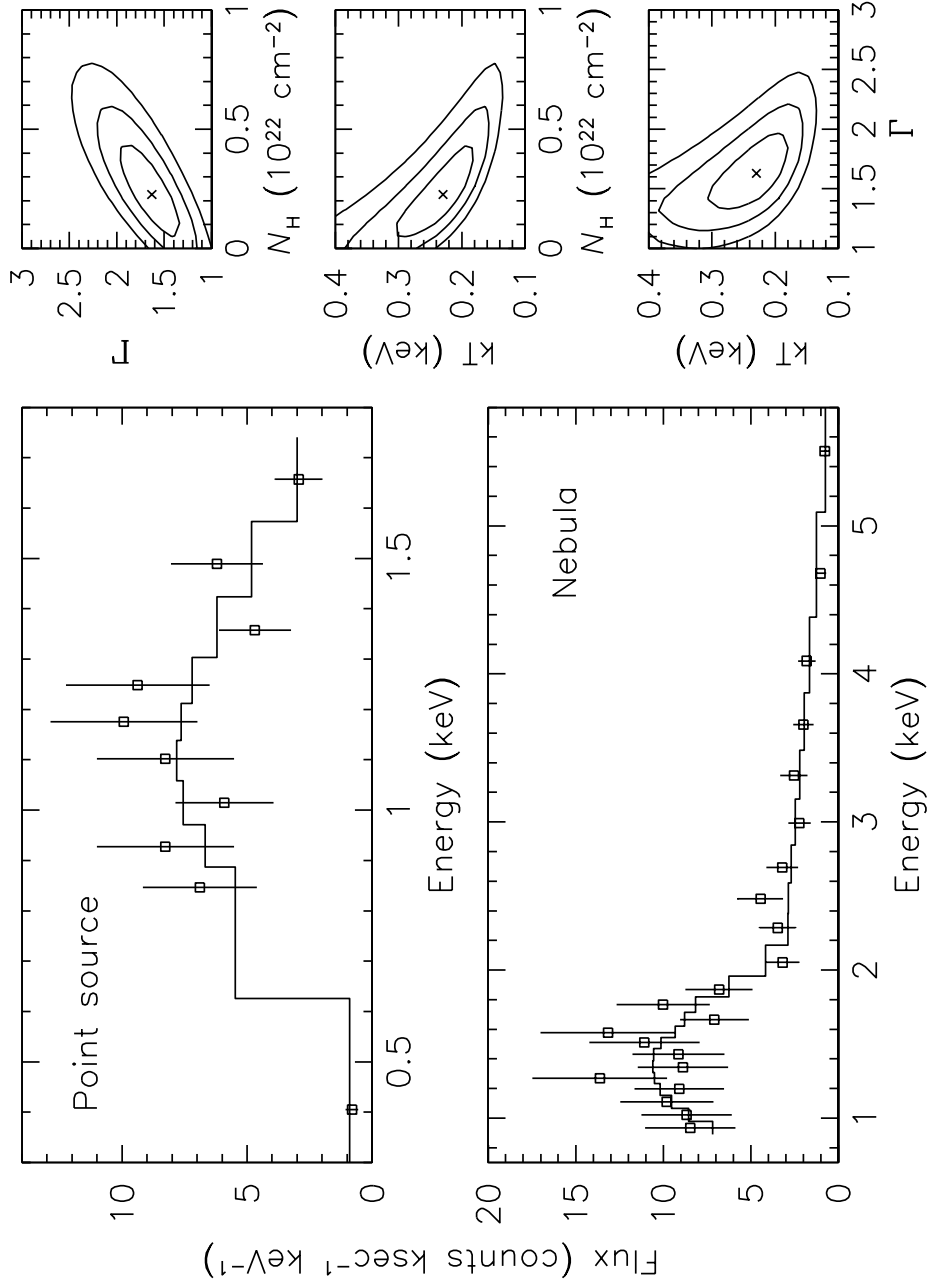


Fig. 5.— Photon flux spectra of the unresolved X-ray source (*top left panel*) and surrounding nebula (*bottom left*), fit simultaneously to blackbody and power-law models respectively, with a common neutral-hydrogen absorption ( $N_{\text{H}}$ ) parameter. To the right, projections of  $\chi^2$  in three planes of interest are plotted as contours representing 1, 2, and  $3\sigma$  uncertainties in the parameter values, where  $kT$  is the blackbody temperature of the point source and  $\Gamma$  is the photon index of the nebula’s power-law spectrum.